Metadata of the chapter that will be visualized online

Series Title	
Chapter Title	Shape-Based Detection of Cortex Variability for More Accurate Discrimination Between Autistic and Normal Brains
Chapter SubTitle	
Copyright Year	2011
Copyright Holder	Springer Science+Business Media, LLC
Corresponding Author	Family Name	El-Baz
	Particle	
	Given Name	**Ayman**
	Suffix	
	Division	Department of Bioengineering, Bioimaging Laboratory
	Organization	University of Louisville
	Address	304 Lutz Building, 40292, Louisville, KY, USA
	Email	aselba01@louisville.edu
Author	Family Name	Nitzken
	Particle	
	Given Name	**Matthew**
	Suffix	
	Division	Department of Bioengineering, Bioimaging Laboratory
	Organization	University of Louisville
	Address	304 Lutz Building, 40292, Louisville, KY, USA
	Email	
Author	Family Name	Casanova
	Particle	
	Given Name	**Manuel**
	Suffix	
	Division	Department of Bioengineering, Bioimaging Laboratory
	Organization	University of Louisville
	Address	304 Lutz Building, 40292, Louisville, KY, USA
	Email	
Author	Family Name	Khalifa
	Particle	
	Given Name	**Fahmi**
	Suffix	
	Division	Department of Bioengineering, Bioimaging Laboratory
	Organization	University of Louisville
	Address	304 Lutz Building, 40292, Louisville, KY, USA
	Email	
Author	Family Name	Sokhadze
	Particle	

> Please update the contact information for Manuel F. Casanova:
>
> Division: Department of Psychiatry
> Address: 500 S Preston St, 40292, Louisville, KY, USA

Given Name	**Guela**
Suffix	
Division	Department of Bioengineering, Bioimaging Laboratory
Organization	University of Louisville
Address	304 Lutz Building, 40292, Louisville, KY, USA
Email	

Abstract   Autism is a complex developmental disability that typically appears during the first 3 years of life, and is the result of a neurological disorder that affects the normal functioning of the brain, impacting development in the areas of social interaction and communication skills. Early detection allows for treatments to be attempted, thus minimizing the impact of the autism on the individual. Given currently available diagnostic instruments, autism and other pervasive developmental disorders are difficult to detect in very young children. While shape based statistical analysis methods for autism are still in their early stages, current results show positive outlooks on the ability to detect differences between autistic and non-autistic patients. A framework is proposed that is capable of taking two-dimensional images from a standard medical scanner, and be able to construct a three-dimensional representation of the object and examine it through combination of its weighted linear spherical harmonics. The desired outcome is that a distinction can be made between the analysis of autistic and non-autistic brain data. The reconstruction analysis process involves linearly combining spherical harmonics of the corresponding mesh. It was expected that due to the complexity of the brain of an autistic subject it would require more iterations of reconstruction to reach convergence of the same error level as compared to the brain of a non-autistic subject. This was confirmed by the data. Using this method of analyzing the data a significant difference can be demonstrated between groups of examined subjects. The research clearly demonstrates that the non-autistic subjects' data converges both faster and with a lower rate of error level than the data taken from a person with autism.

Chapter 7
Shape-Based Detection of Cortex Variability for More Accurate Discrimination Between Autistic and Normal Brains

Matthew Nitzken, Ayman El-Baz, Manuel F. Casanova, Fahmi Khalifa, and Guela Sokhadze

Please rearrange the authors as follows:
Matthew Nitzken, Manuel F. Casanova, Fahmi Khalifa, Guela Sokhadze, and Ayman El-Baz

Abstract Autism is a complex developmental disability that typically appears during the first 3 years of life, and is the result of a neurological disorder that affects the normal functioning of the brain, impacting development in the areas of social interaction and communication skills. Early detection allows for treatments to be attempted, thus minimizing the impact of the autism on the individual. Given currently available diagnostic instruments, autism and other pervasive developmental disorders are difficult to detect in very young children. While shape based statistical analysis methods for autism are still in their early stages, current results show positive outlooks on the ability to detect differences between autistic and non-autistic patients. A framework is proposed that is capable of taking two-dimensional images from a standard medical scanner, and be able to construct a three-dimensional representation of the object and examine it through combination of its weighted linear spherical harmonics. The desired outcome is that a distinction can be made between the analysis of autistic and non-autistic brain data. The reconstruction analysis process involves linearly combining spherical harmonics of the corresponding mesh. It was expected that due to the complexity of the brain of an autistic subject it would require more iterations of reconstruction to reach convergence of the same error level as compared to the brain of a non-autistic subject. This was confirmed by the data. Using this method of analyzing the data a significant difference can be demonstrated between groups of examined subjects. The research clearly demonstrates that the non-autistic subjects' data converges both faster and with a lower rate of error level than the data taken from a person with autism.

A. El-Baz (✉)
Department of Bioengineering, Bioimaging Laboratory, University of Louisville, 304 Lutz Building, Louisville, KY 40292, USA
e-mail: aselba01@louisville.edu

7.1 Introduction

Autism is a complex developmental disability that typically appears during the first 3 years of life, and is the result of a neurological disorder that affects the normal functioning of the brain, impacting development in the areas of social interaction and communication skills. Difficulties can be identified in both children and adults with autism. The symptoms are identifiable in verbal and nonverbal communication, social interactions, and leisure or play activities. The classic form of autism involves a triad of impairments, these are typically in social interaction, in communication and the use of language, and in limited imagination as reflected in restricted, repetitive, and stereotyped patterns of behavior and activities [1].

The reported incidence of autism spectrum disorders has increased markedly over the past decade [2]. It is believed that autism affects the information processing found in the brain through the alteration of nerve collections and their synapses [3]. From Congress to popular media, speculation is increasing that more children have autism than ever before. The three classifications of autism include autism spectrum disorders (ASD), Asperger syndrome (AS) and pervasive developmental disorder (PDD) [4].

A study done in 2008 by Rapin and Tuchman [5], shows that autism is now recognized in 1 out of 150 children making it a prevalent disorder [5, 6]. Additional studies by DiGuiseppi show a high prevalence among screened American children with as high as 6.4% of screened children showing at least a mild form of an autistic spectrum disorder [7, 8]. According to the Centers for Disease Control and Prevention (CDC) in 2009, about 1 in 110 American children will fall somewhere in the autistic spectrum. Although the cause of autism is still largely not clear, researchers have suggested that genetic, developmental, and environmental factors may be the cause or the predisposing effects towards developing autism [9].

There are other mathematical relationships between incidence and prevalence. An important nuance about prevalence is that its accuracy is only as good as the degree to which each individual who actually has the condition is counted (the numerator or top number of the fraction), and the completeness with which the "general" or other population has been counted (the denominator or bottom number of the fraction.) Accuracy in these two figures can be hard to achieve. In fact, there are no scientifically based epidemiological prevalence estimates for ASD in the USA at this time. Federal agencies have, however, called upon researchers to submit proposals that will develop better prevalence rates [4].

Until research in the USA results in more accurate figures, the National Institutes of Health (NIH) have suggested the following prevalence rates for ASD based upon research in other Westernized, developing nations:

- 10/10,000 people with "classic" autism
- 20/10,000 people with ASD, including PDD
- 50/10,000 people with ASD, including PDD and Asperger syndrome

These estimates are inclusive; that is, the third estimate includes people in the first two groups. This means that in a given large population, on average 0.5%, one-half percent of the population could be diagnosed with an ASD [4].

Early detection allows for treatments to be attempted, thus minimizing the impact of the autism on the individual. Given currently available diagnostic instruments, autism and other PDD are difficult to detect in very young children. This may be due to several factors: presentation of symptoms varies from case to case; social and language deficits and delays may not be identified until the child is given the opportunity for peer interaction in preschool, low incidence leads to a low index of suspicion, and motor milestones are usually unaffected. Furthermore, there is no standard and easily administered screening instrument for young children. For all of these reasons, pediatric evaluations rarely identify autism before the age of three. However, evidence indicates that there is a large gap between the age of the child at the parents' first concern, the age of the first evaluation, and the age of a definitive diagnosis [8]. Parents are typically first concerned between the ages of 15 and 22 months (earlier for children who have co-morbid mental retardation), but the child is often not seen by a specialist until 20–27 months [14]. In addition, there is often further delay between the first visit to a specialist and a definitive diagnosis. However, evidence shows that this delay in diagnosis causes additional distress to parents, as well as wasting valuable intervention time, indicating that professionals in the field of autism need instruments to aid in the detection of autism in very young children [10].

Some forms of autism merely result in the individual exhibiting low social interaction, but more severe forms can result in severe mental retardation. These individuals may be prone to self-injuring and aggressive behavior. There is no current cure for any forms, of autism. However, educational, behavioral, or skill-oriented therapies were designed to remedy specific symptoms in each individual. Such therapies can result in a notable improvement for the individual, especially when begun at a young age [10].

7.1.1 Neuropathology of Autism

In identification of autism, the analysis of the neuropathology is important. The role of single-stranded microdeletions and epigenetic influences on brain development has dramatically altered our understanding of the etiology of the autisms. Recent research has focused on the role of synapse structure and function as central to the development of autism and suggests possible targets of interventions. Brain under connectivity has been a focus in recent imaging studies, and has become a central theme in conceptualizing autism. Despite increased awareness of autism, there is no "epidemic" and no one cause for autism. Data from the sibling studies are identifying early markers of autism and defining the broader autism phenotype [5].

The three sections of the brain analyzed are the gray matter, the white matter, and the corpus callosum. Examination of the individual sections shows significant

114 changes to the neuropathology of autistic individuals, suggesting a higher complex-
115 ity in the autistic brain than the normal brain [11].

116   The gray matter is the brain cortex that contains the nerve cells responsible for
117 routing sensory or motor stimuli to interneurons of the central nervous system. In
118 autistic individuals Abel et al. [12] identified a decreased gray matter volume
119 relative to a control group in the right paracingulate sulcus, the left inferior frontal
120 gyrus, and an increased gray matter volume in amygdala and periamygdaloid
121 cortex, middle temporal gyrus, inferior temporal gyrus, and in regions of the
122 cerebellum. Additionally Boddaert et al. [13] found significant decreases of gray
123 matter concentration in the superior temporal sulcus when comparing autistic child
124 patients to normal child patients. The autistic children also demonstrated a decrease
125 in white matter concentration located in the right temporal pole and in the cerebel-
126 lum. Herbert et al. [14] applied a voxel-based-morphometry (VBM) approach to
127 male patients between the ages of 7 and 11 years and showed that those with autism
128 had a significantly larger volume of cerebral white matter (CWM) while cerebral
129 cortex and hippocampus–amygdala had smaller volumes. The corpus callosum is
130 largest single fiber bundle in the brain and is responsible for connecting the two
131 hemispheres of the brain. It has been proposed that there are significant differences
132 between the CC of autistic and normal patients [15, 16].

133   The concept that the cerebellum might play a role in the coordination of attention
134 in a fashion analogous to the role it plays in motor control and that in autism,
135 cerebellum mal-development is a consistent feature that renders the child unable to
136 adjust his or her mental focus of attention to follow the rapidly changing verbal,
137 gestural, postural, tactile, and facial cues that signal changes in a stream of social
138 information [17]. Such cues signal the normal child to move his or her "spotlight of
139 attention" from one source of information (e.g., auditory) to another (e.g., visual).
140 This process involves disengaging attention from one source and then moving and
141 reengaging it on another (i.e., inhibition of one source and enhancement of another).
142 To selectively adjust the focus of attention, the nervous system must quickly and
143 accurately alter the pattern of neural responsiveness to sensory signals – from an
144 enhanced neural response to certain stimuli (e.g., vocalizations) to an enhanced
145 response to other stimuli (e.g., gestures), and from inhibited neural response to
146 some stimuli to inhibited response to others [18, 19].

147 ## 7.1.2   Related Work

148 One method of early detection intervention, utilizes medical providers to screen
149 children using the Modified Checklist for Autism in Toddlers (M-CHAT) as they
150 were referred for early intervention services. The M-CHAT is designed to screen
151 for early identification of autism spectrum disorder (ASD) in toddlers over the age
152 of 12 months. Ideally, it is given at the 18–24 month well baby check. Parents
153 complete the items on the checklist independently or by interview. Meeting the
154 criteria suggests the risk of ASD and indicates a positive diagnosis for autism. The

purpose is to survey parents to determine how their child responds to varied stimuli 155
from toddler locomotion to a child's reaction to other people. M-CHAT users also 156
incorporate the M-CHAT Follow-up Interview into the screening process, given 157
that recent findings demonstrate that the interview greatly reduces the false positive 158
rate, which avoids unnecessary referrals [14]. Therefore, these children were 159
considered to be at risk for a developmental disorder, but none had received any 160
specific diagnoses and none had received more than several weeks of minimal 161
intervention services. 162

In new experiments at Yale University, the researchers studied a group of 163
2-year-olds with autism, as well as typically developing children with developmen- 164
tal disabilities other than autism. The Yale program of research focuses on mechan- 165
isms of socialization and their disruption in the autism spectrum disorders. This 166
work includes a close collaboration with Warren Jones in the development of novel 167
techniques to quantify social processes using eye-tracking technologies with a view 168
to visualize and measure the ontogeny of social engagement. New data analysis 169
strategies have been used with children, adolescents, and adults with autism 170
spectrum disorders revealing abnormalities of visual scanning behaviors when 171
viewing naturalistic social approaches and situations. In this study autistic children 172
showed a preference for audiovisual synchronicity in the use of "pat-a-cake" 173
videos, while the other children were more interested in the figure's movements 174
regardless of audiovisual synchronicity. That pattern could be a clue about brain 175
development and early signs of autism [20–23]. 176

Dr. Klin of Yale University explains that within a few days after birth, normal 177
developing children prefer watching biological motion, the movement of living 178
beings, such as their parents, and that preference is an important survival skill and a 179
building block for relationships [21]. But Klin's group found that autistic children 180
were more interested in "non-social contingencies," which are synchronicities that 181
do not have any social meaning, like two balls colliding and making a sound, or a 182
stone falling when someone drops it [20]. 183

Researchers hope that a simple brain scan performed in infants and toddlers can 184
presage the development of autism, leading to early detection and early interven- 185
tion. The test involved using functional magnetic resonance imaging (MRI) to 186
measure brain responses to spoken words in sleeping children. For this study, Dr. 187
Eyler and her colleagues monitored the brain activity of 30 children with an autism 188
spectrum disorder (aged 14 months to 46 months) and 14 "typical" children of 189
roughly the same age [24]. 190

Children slept in the MRI machine while researchers read them bedtime stories. 191
This allowed the investigators to see which parts of the brain were being activated in 192
typical children vs. children with autism. "In the typically developing children, both 193
sides of the brain involved in language processing were activated. In the youngest 194
children, the activation was about equal in both the right and left hemisphere, while 195
in the older children, activity became more pronounced on the left side, which is 196
similar to adult patterns and to be expected," Dr. Lisa T. Eyler explained. But in the 197
autistic children, there was slightly more right hemisphere response than left 198
hemisphere, and there was no change in activity across the age range [24]. 199

David G. Amaral stated that "this leads to the conclusion that, in many children with autism, there are alterations either in structure growth or connectivity of the brain, but we really don't understand the implications of that for core features of autism, one of which is the problem with communication. This provides more evidence for abnormal connectivity in the brain." [24].

Further analysis of neurological MRI scans has been pursued in automated computer analysis of specific components of the brain. Approaches by El-Baz et al. [11] examine the shape model comparison between the corpus callosum in individuals with and without autism. This analysis focuses on comparison of the three-dimensional voxel positioning. In such an automated technique, specific areas of MRI scan images are extracted. These images are then placed in a stack to recreate a volume of the image. The difference between regions of this volume can be statistically measured. While statistical analysis methods are still in their early stages, current results show positive outlooks on the ability to detect differences between autistic and normal patients based on voxel-based analysis. The positive findings from automated analysis research provide the basis for the research done in this chapter.

There are many different methods that can be used to examine objects for difference. In the area of autism detection and analysis, Gyral Window Index (GWI) and volumetric descriptions of brain structures (volume analysis) are the most common ones.

GWI analysis involves counting the gyrations found along the brain in various areas and comparing these counts to make an assumption. This technique is heavily prone to error in that brains that differ in shape and complexity may show little to no difference and brains of similar shape and complexity could show a large difference.

Volumetric descriptions of brain structures examine the volume of an object. This is also commonly known as volume analysis. In this the volumes of objects are compared. While this does relay important information, it is not optimal for examining a complex organ. Imagine that you have two bowls. One of these is shaped like a large flat saucer and the other is shaped like a very thin vase. Assume that both of these will hold the same amount of liquid when filled. This example illustrates the flaws of volume based analysis on an object. While the volumes are identical for the two objects, the shape and complexity is drastically different. An example of this type of phenomenon can be seen in Fig. 7.1 illustrated by a clear plastic geometry set.

Shape analysis is an alternative method to the previous two. In these the shape is represented by a complex mesh of nodes. These nodes fall within respective areas on the surface and can be compared to one another to determine differences. Instead of examining the volume or visual changes along the cortex of the brain the locations of points on the brain are examined and compared based on their locations in space. This examination performs a comparison between specific points as illustrated in Fig. 7.2. It is important to maintain strict rules on construction and examinations of objects when using this technique to ensure accuracy. This chapter will focus on a framework for the analysis of the cortex using shape analysis through the construction and examination of spherical harmonics.

Fig. 7.1 Containers that all hold an identical volume with dramatically different shapes
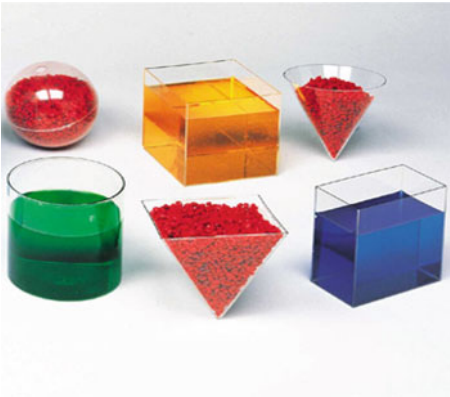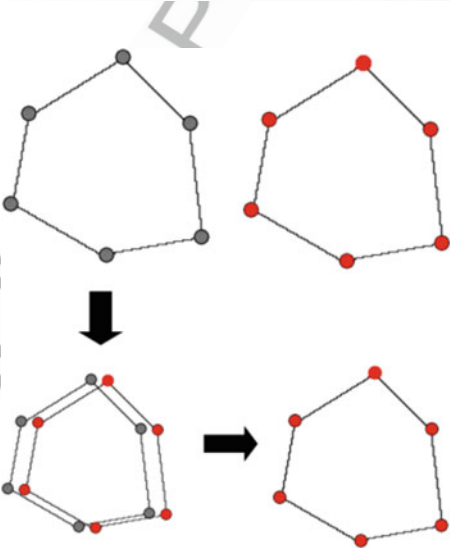

Fig. 7.2 Illustrating the comparison between points representing an object in shape analysis instead of examining the object as one volumetric entity

7.2 Methods

The proposed analysis system is subdivided into the parts found in Fig. 7.3. This section will primarily cover the second and third rows in the flowchart which pertain to three-dimensional mesh construction and to the analysis of a mesh using spherical harmonics. The initial data consists of segmented MRI images of data.

First, the raw recorded image data is passed through a system to remove the skull from the image. This is done using the software called MRIcro developed by Chris Rorden from the Neuropsychology Lab and Georgia Institute of Technology in Altlanta, GA [25–28]. This software examines the raw image and removes and pixel data pertaining to the skull leaving only brain matter remaining as shown in
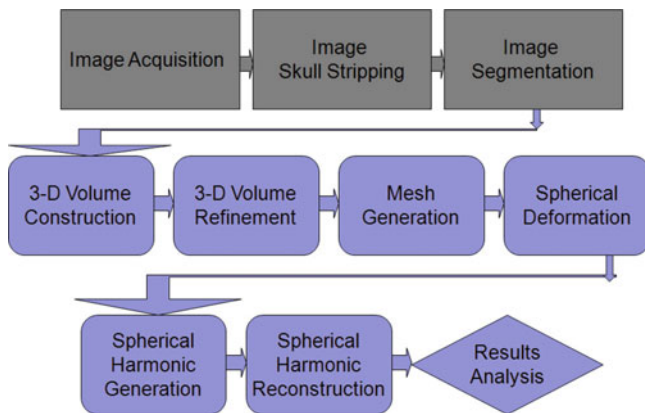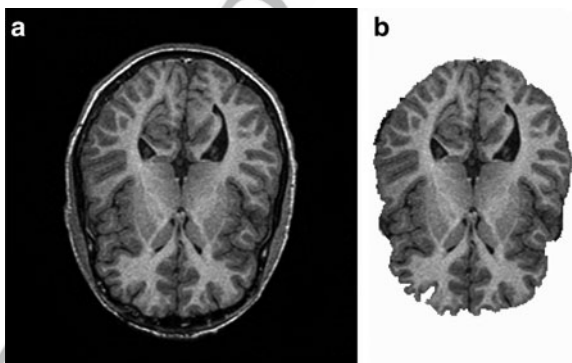
Fig. 7.3 Flowchart of the proposed analysis system

Fig. 7.4 (**a**) Typical MRI image, (**b**) image after removal of skull from around the brain using MRIcro

256 Fig. 7.4. After this the image is segmented to a binary representation. The image is
257 inverted so that the brain received by the framework has a black background and the
258 brain data is the white area.

259 For each image, a black pixel represented the background or portions of the
260 image where no data existed, and the white pixels represented areas where data
261 existed (Fig. 7.5). Often images formats do not store data in binary form and data is
262 stored using a variation of a grayscale format. The individual pixel values range
263 from 0 to the maximum grayscale value (in many cases this value was 255 and
264 represented a white pixel.) It can be assumed then that any pixel with a value greater
265 than zero would constitute a pixel containing data. Setting all pixels to the desired
266 limits can be accomplished by dividing the matrix by the maximum value and then
267 taking using a ceiling command on the data.

268 After each image is converted to a binary representation, the images are assem-
269 bled in a three-dimensional matrix stack. Each matrix is represented by an X, Y, and
270 Z dimension. The X dimensions represent the rows in an image, the Y dimension
271 represents the columns in an image, and the Z dimension represented the layers in

Fig. 7.5 Examples of segmented brain data used as input data

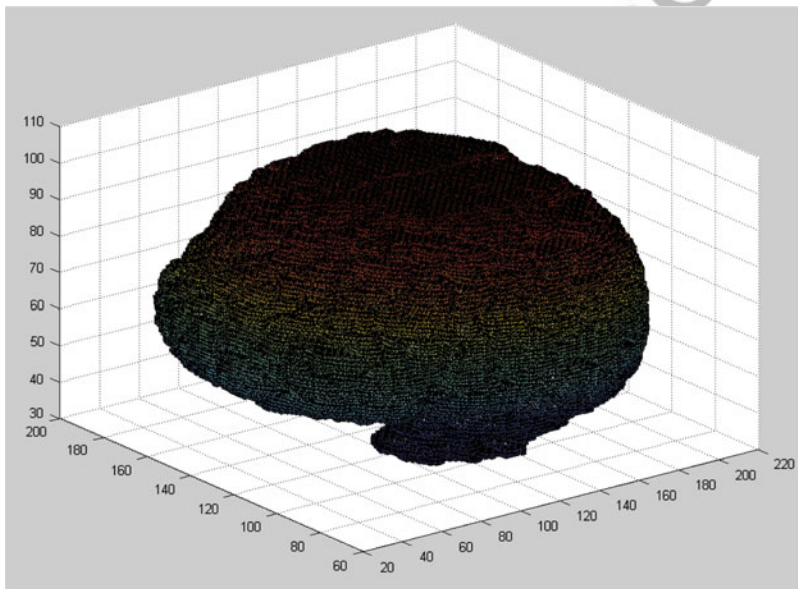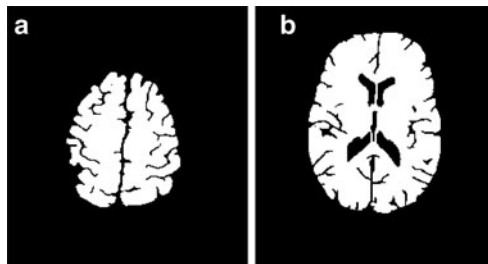**Fig. 7.6** Three-dimensional binary representation of a brain

the volume, with each layer encompassing a separate distinct image. Each coordinate (x, y, z) represented a single voxel in three-dimensional space and the combination of the voxels is a rough three-dimensional representation of the object to be analyzed. Figure 7.6 illustrates a generic representation of a three-dimensional volume as viewed using Matlab. 272 273 274 275 276

In this framework the images are loaded into the memory without preprocessing to remove holes in the images. This is done because when the images are compiled into a shape in three-dimensional space, holes can be created by the placement of layers on top one another. It is a simpler process to simply execute an algorithm to remove these holes using one processing step than to perform both pre and post processing on the volume. While initially the decision was made to remove all holes in the two-dimensional images prior to being loaded into the program, this proved ineffective after the images were placed in a three-dimensional volume. To remove these holes from the image, a hole detection algorithm can be used. 277 278 279 280 281 282 283 284 285
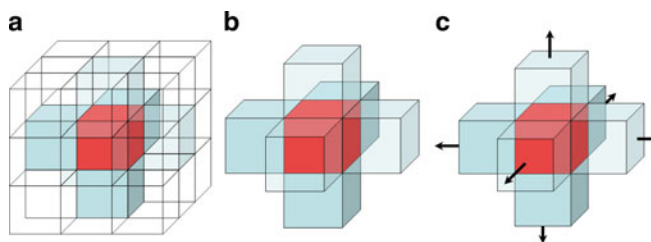
Fig. 7.7 (**a**) The original cube of pixels, (**b**) showing the starting neighbor pixels in the six cardinal directions, (**c**) the outward directions of movement for the detection iterations

286 The algorithm begins by loading the images into the three-dimensional volume
287 matrix as previously described. After creating the three-dimensional volume
288 matrix, an iterative pass is made across the X, Y, and Z axis of the volume using
289 the Matlab "fillholes" command. To accomplish this, a two-dimensional image
290 slice is removed on each plane of the volume. This image slice was then passed
291 through the "fillholes" algorithm, and the modified image slice was reinserted into
292 the volume. In this way, the holes were removed from the two-dimensional
293 representations in the X, Y, and Z directions.

294 Following this procedure, additional small holes not removed using the previous
295 method are scanned for and removed. To remove these additional holes, each
296 individual pixel is iterated in the three-dimensional matrix. For each pixel, it is
297 calculated if there was a pixel belonging to the image in the $\pm X$, $\pm Y$, and $\pm Z$
298 directions between the origin pixel and the edge of the volume. In Fig. 7.7a, the
299 origin pixel is defined as the red pixel, the blue neighbor pixels are the $\pm X$, $\pm Y$, and
    $\pm Z$ directional pixels, and the clear pixels represent unchecked points. Figure 7.7b
301 shows the same image with the unchecked pixels removed for easier visibility.
302 From the image points, outgoing vectors were tested in each of the six directions.
303 Figure 7.7c illustrates the path of testing that each neighbor pixel would expand
304 from towards the outer edge. If a pixel value of 1 is found in a given direction, a
305 value of true is marked for the boolean corresponding with that direction.

306 If a pixel is found radiating out in all six directions, it is determined that the pixel
307 was a hole in the image. A pixel that does not contain pixels surrounding it on all six
308 sides is ignored. This procedure is repeated until holes are removed from the image.
309 This is often accomplished in a single iteration. To ensure that the volume is clean,
310 an additional iteration is repeated that verifies that no holes remain in the volume.

311 7.2.1 Mesh Generation

312 Once the three-dimensional volume has been properly constructed, the mesh can be
313 generated. In this framework, the mesh generation is performed using a modified
314 version of the iso2mesh Matlab based mesh generation system, written by Qianqian
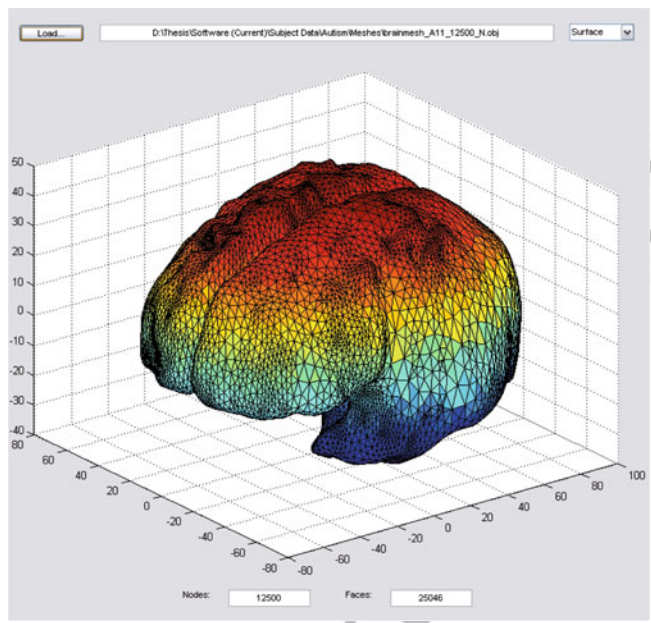
Fig. 7.8 Mesh render for the cortex of an autistic person

Fang and David Boas [29, 30]. A sample mesh render is illustrated in Fig. 7.8. This 315
system is built on the CGAL Delaunay Triangulation mesh engine. This is a 316
nonrigid mesh generation engine, and points are not constrained to contain a 317
specific number of neighboring nodes. The modifications to the original iso2mesh 318
code are to enable restriction of node counts and to generate a raw nonprocessed 319
mesh. The restriction of node counts is important to ensure that objects being 320
compared have the same properties. The raw mesh is recovered from the iso2mesh 321
package before any of the post processing and surface analysis is performed on it. 322
For this framework, these alterations are not necessary and can lead to complexity 323
problems in the mesh. 324

The data received from the mesh generation is a collection of nodes and 325
triangulations. The nodes matrix is of dimensions $3 \times N$, and the triangulations 326
matrix is of dimensions $4 \times T$, where N is the maximum allowable amount of nodes 327
and T varies based on the positions used by the mesh engine and the triangulations 328
created between points. The combination of three triangulation points connected 329
with one another represents a face found on the corresponding mesh and each row 330
in the triangulations matrix contains data representing a unique face. The fourth 331
column in the triangulation matrix is a boolean value representing that the face 332
connectivity at this point exists. Following mesh creation, all values in this fourth 333
column will be equal to true and this column can thus be removed to create the 334
traditional $3 \times T$ representation found in a mesh triangulation matrix. 335

Once the initial mesh is created, it is necessary to reposition it in three- 336
dimensional space and to resize the mesh to appropriate proportions. The centroid 337

338 of the mesh is calculated in the X, Y, and Z directions. Using the coordinates of the
339 centroid, the mesh is repositioned so that it is centered on the origin in three-
340 dimensional Cartesian space ($x = 0$, $y = 0$, $z = 0$). Because of data acquisition
341 limitation the original mesh is not scaled properly. It is necessary then to appropri-
342 ately resize the mesh using the original image slice acquisition scaling. The mesh
343 coordinates are then repositioned according to the X, Y, and Z magnification
344 parameters of the scanner used to acquire the images. The X and Y planes are
345 multiplied by a magnification factor of 0.93 in this example, taken from the MRI
346 scanner acquisition parameters. The Z plane is scaled by a factor of 1.5 in this
347 example, the distance between slices taken during MRI acquisition. The result is a
348 properly scaled mesh that is centered around the origin in three-dimensional space.
349 The raw mesh generation returns a node and face cluster where vertex points
350 contain a large amount of noise. To remove this, noise a vertex-based anisotropic smoo-
351 thing filter is applied to the data. The filter performs a low-pass filter Laplacian
352 smoothing algorithm across the exterior of the mesh. The low-pass filter Laplacian
353 smoothing algorithm used in this framework is based on code written by Zhang and
354 Hamza [31]. The smoothing algorithm is applied iteratively three times during the
355 procedure, and is configured to smooth at a minimal value with each pass. The final
356 mesh is accurately scaled and correctly positioned in three-dimensional space and
357 contains smooth and accurate contours representing the various locations found on
358 the cortex.

359 The file format chosen to save the mesh data in this framework is the Wavefront
360 OBJ format, developed by Wavefront Technologies. The standardized Wavefront
361 OBJ format is used because it is a common mesh file representations used in a
362 majority of commercial and open-source application mesh analysis applications
363 and will allow for potential future integration of the framework with third-party
364 software. Custom algorithms have been written to write and save meshes in this
365 format in a way that is universally compatible. The algorithms used follow all
366 standard guidelines for the common Wavefront OBJ format.

367 ## 7.2.2 Spherical Deformation

368 Following the generation of a stable, hole-free initial mesh, it was necessary to
369 generate a corresponding unit sphere. The accuracy of the sphere creation is relative
370 to the accuracy of the statistical analysis. There were several techniques attempted
371 including Cartesian and spherical registration methods.

372 The initial attempt to create a unit sphere involved simply inflating the original
373 mesh into a unit sphere. This technique was done by reducing all points in the mesh
374 to a maximum distance of 1.0 from the origin. Once the mesh had been scaled, all
375 points with a value less than 1.0 were up scaled to a value of 1.0. This inflation
376 technique resulted in numerous problems, with the most problematic being vertex
377 overlap and poor distribution of points. The natural shape of the brain sulci and the
378 valley located between hemispheres in the brain created this overlap by inverting

Please change this to read:

To remove this noise, a vertex-based...

points and face connectivity, as they were forced to the outer edges of the inflated sphere. This occurred due to the fact that multiple points existed along the same or incorrect θ and φ angles in spherical space.

In the creation of a unit sphere, it became imperative that all points remain in their correct orientation with their neighbor points during the deformation process. This means that during deformation, the triangulation connections could not become crossed. A unit sphere that contained crossed triangulations produced an erroneous spherical representation. This is because during calculation of the harmonics it assumes that the detected neighboring nodes are truly the neighbor nodes for a given vertex. If the points become misplaced or shifted to an erroneous location away from its true position than a neighboring node may appear to be falsely connected to additional nodes. The spherical harmonics are based on angular values, and points with incorrectly crossed angles caused the system to produce poor resultant data making a spherical reconstruction not possible.

The accuracy of the spherical representation was also based on the distribution of the vertex coordinates throughout the sphere and the accuracy to it being a true unit sphere. A sphere with clusters of vertices and other areas of sparse vertex placement produced significantly more error and had a greater difficulty converging. The ideal spherical representation will have all vertices spaced equidistant from one another across the surface of the sphere. While it is possible to perform an analysis using an improperly spaced unit sphere, the results were less than desirable. The original method leaves large clusters of vertices around areas of significant sulcus curvature in the brain.

The process, used in the creation of a unit sphere is a multiple phase deformation technique, created for the purpose of deforming the brain meshes. Before running the spherical deformation, the brain was heavily smoothed using a Laplacian based smoothing algorithm. The mesh was loaded into the freely available software, MeshLab v1.2.3b written by Paolo Cignoli [32, 33]. It was determined through trial and error that an average smoothing of 400 iterations per 12,500 nodes deformed the mesh so that no existing points in the mesh could be found residing on the same θ and azimuth angles, when examined in spherical coordinate space (Fig. 7.9). MeshLab was used to improve processing speed during the smoothing phase. The comparable Matlab algorithm took approximately 30 seconds to run one
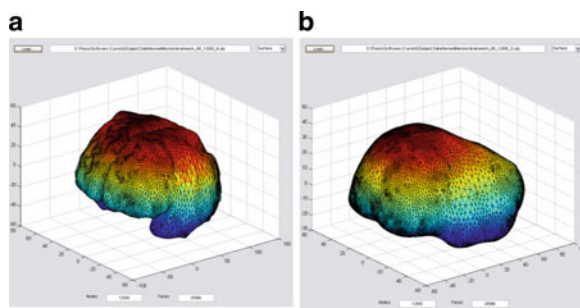

Fig. 7.9 (**a**) An original brain render and (**b**) the render after 400 iterations of Laplacian smoothing

412 complete Laplacian smoothing pass. The same algorithm run in MeshLab was
413 capable of performing 2000 Laplacian smoothing passes in slightly under one
414 minute.

415 **Algorithm 1: Spherical Deformation Algorithm**

416 1. *Deformation of original mesh into smoothed mesh model.*
417 2. *Expansion of smoothed mesh model distances to distance of unity sphere.*
418 3. *Application of attraction–repulsion algorithm for node positioning refinement*
419 *on expanded mesh.*
420 4. *Expansion of refined mesh model distances to distance of unity sphere.*

421   The Spherical Deformation Algorithm was used to transform the shape of a
422 constructed mesh to that of a unity sphere. In the Laplacian deformation phase, the
423 brain is smoothed until all curves, peaks, and valleys of the cortex are flattened
424 across the brain. This ensures that no more than one point will be found for a given
425 set (azimuth and θ angles) of spherical coordinates. This mesh is then resaved as a
426 smooth mesh object which will be loaded for the second through fourth phases.

427   The unit sphere distance deformation involves inflating the smoothed mesh to
428 the distance of a unit sphere. To increase the speed of the spherical inflation it is
429 necessary to manipulate the mesh in the spherical coordinate domain. The Cartesian
430 mesh is first converted to spherical coordinates using the *cart2sph* command in
431 Matlab. This returns a θ angle, azimuth (φ) angle, and R distance for each point in
432 the mesh. The R distance is removed and replaced with a matrix of the same size
433 with all values equal to 1.0. The coordinates are then reconverted to Cartesian using
434 the *sph2cart* command in Matlab. This provides a fast and effective conversion that
435 is extremely efficient, because it requires no iterative processing and does not
436 involve examining each node individually or performing any distance calculations.
437 These inflated points are then passed on to the third phase.

438   In the third phase, the attraction–repulsion algorithm is used to refine the inflated
439 sphere. The attraction–repulsion algorithm is based on a standard spring algorithm.
440 The algorithm was inspired by a concept used in Graphic Art Design for inflating
441 objects. The purpose of this algorithm is to reposition the nodes in the mesh. After
442 the second phase of the spherical deformation, there are large clusters of nodes
443 spaced near one another in areas of the mesh that contain a high density of nodes.
444 Looking at the mesh, it is possible to see large clusters near the lower lobes of the
445 brain and around complex areas. As previously mentioned, it is necessary to evenly
446 space the nodes across the sphere. To accomplish this, the attraction–repulsion
447 algorithm was created.

448   The attraction–repulsion algorithm is composed of two steps, the attraction
449 step and the repulsion step. Each node is altered by being processed in the
450 attraction step and then the repulsion step. In the attraction step, the node is
451 altered based on its neighbor nodes. The distance between a node and each of its
452 neighbor nodes is calculated. The node is then pulled based on numerical weight-
453 ing, so that it becomes centered between its neighbors. The attraction for iteration
454 i is defined as:

AU2

$$A_{i+1} = A_i + (\overline{Q_N P_J})(D^2)(0.01) + (\overline{P_J Q_N})\left(\frac{0.00001}{D}\right), \tag{7.1}$$

$$1 \le j \le \text{number of nodes}, \quad 1 \le N \le \text{number of neighbors}$$

where A_{i+1} represents the new node coordinate and A_i is the original node coordi-   455
nate. P represents the original coordinate of the unmodified node that is and Q is the   456
coordinate of neighbor node N. The distance (D) from P to Q is a three-dimensional   457
Euclidean distance.   458

After the node has been centered between its neighbors it is processed in the   459
repulsion step. Here the node is slightly readjusted by every node in the mesh. Each   460
node minimally repels one another so that the nodes do not cross or touch. The   461
repulsion is defined as: 462

$$R_{i+1} = R_i + (\overline{Q_k P_J})(T)\left(\left(\frac{1.5}{(\overline{Q_k P_J})^2}\right)\left(\frac{1}{2N}\right)\right), \tag{7.2}$$

$$1 \le j \le \text{number of nodes}, \quad 1 \le k \le \text{number of nodes}$$

where $R_i + 1$ represents the new node coordinate and R_i is the original node   463
coordinate. N represents the total number of nodes in the mesh. T is a value between   464
0 and 1 and stands for the time step of the algorithm. A larger time step enables the   465
algorithm to converge faster, but increases the chance of error as nodes are capable   466
of moving larger distances.   467

This algorithm also causes an inflation effect to occur during repeat iterations as   468
each node is gently repelled from interior angles by nodes opposite it on the unit   469
sphere. Because there are no nodes outside the unit sphere to repel the nodes back   470
toward the center this inflation occurs. This step is repeated several times until a   471
satisfactory node distribution is reached (Figs. 7.10 and 7.11). Once the attraction–   472
repulsion algorithm has completed, the nodes are more evenly spaced on the sphere.   473
Due to the previously described interior repulsion, the sphere is also much larger   474
than a unit sphere of radius 1 at this point. To alleviate this phenomenon, the unit   475
sphere distance deformation algorithm is run a second time. While this algorithm   476
does not alter the angular placement of the nodes, it will reduce the R values back to   477
1 for all nodes. This is the same algorithm that is run during phase two. Following   478
this deformation, the newly created unit sphere mesh is written back into a Wave-   479
front OBJ file.   480

7.2.3   Spherical Harmonic Analysis   481

The weighted spherical harmonic representation (weighted-SPHARM) is a surface   482
modeling framework that can be used in encoding cortical shape information. The   483
technique was developed by Moo K. Chung, Kim M. Dalton and Richard J. Davidson.   484

Fig. 7.10 (**a**, **c**) Simple spherical inflations of subject brains. (**b**, **d**) The respective corresponding unit spheres after three iterations of the attraction–repulsion algorithm have been applied
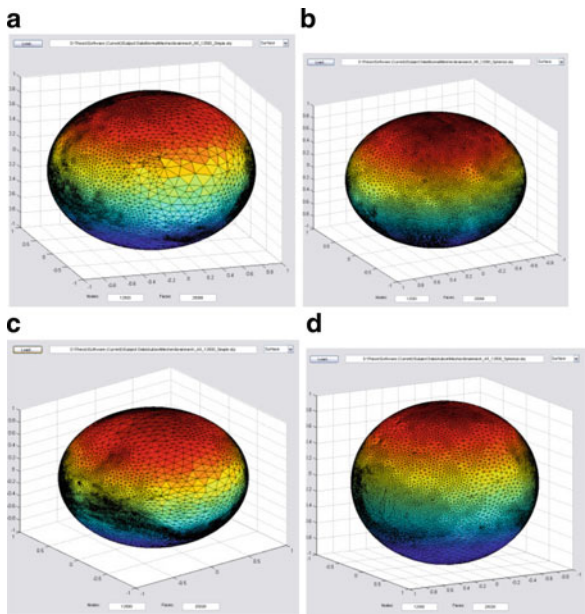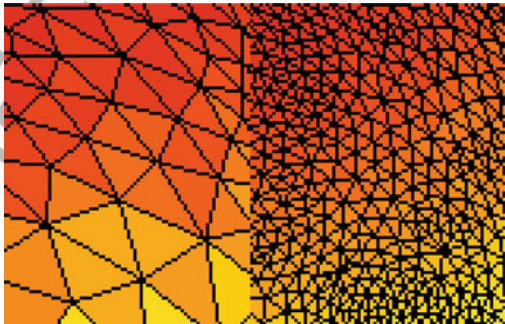

Fig. 7.11 Detailed view of the same region before and after application of the attraction–repulsion algorithm

The weighted-SPHARM representation is a spectral method [34], where a linear combination explicit basis functions is used to represent noisy cortical surface data. The basis expansion corresponds to the solution of an isotropic heat equation on a unit sphere. The result of the weighted-SPHARM is explicitly given as a weighted linear combination of spherical harmonics. This provides a more natural setting for statistical modeling. The representation can be further used in surface registration that reduces the improper alignment of brain sulcus folding patterns between subjects and across hemispheres within a subject.

The system generates harmonics from the original distribution of coordinates. This ensures that the same neighbor nodes are connected in the same order between the original and the reconstructed mesh. The harmonics are specifically generated

from the unique unit sphere corresponding to the original mesh. The original 496
Cartesian coordinate system of the corresponding unit sphere mesh parameterizes 497
a coordinate $v_i = v(x, y, z)$ to spherical coordinates with a polar angle between 498
0 and π and an azimuth angle between 0 and 2π. Each point is then represented 499
as a spherical coordinate that can be expressed as $v_i = v(\theta, \varphi)$. The distance from 500
the origin, or R value, in spherical space is always equal to 1.0 for any given point 501
on a unit sphere [35]. The paper by Chung et al. defines the values of θ and φ for 502
purposes of calculation as: 503

$$\theta_{\text{SPHARM}} = \frac{\pi}{2} - \varphi, \quad \varphi_{\text{SPHARM}} = \pi + \theta. \tag{7.3}$$

The spherical harmonic Y_{lm} of degree l and order m [36, 37] is defined as: 504

$$Y_{lm} = \begin{cases} c_{lm}P_l^{|m|}(\cos\theta)\sin(|m|\varphi), & -l \leq m \leq -1 \\ \frac{c_{lm}}{\sqrt{2}}P_l^{|m|}(\cos\theta), & m = 0 \\ c_{lm}P_l^{|m|}(\cos\theta)\cos(|m|\varphi), & 1 \leq m \leq l \end{cases}, \tag{7.4}$$

$$c_{lm} = \sqrt{\frac{2l+1}{2\pi}\frac{(l-|m|)!}{(l+|m|)!}}, \tag{7.5}$$

where $P_1^{|m|}$ is the associated Legendre polynomial of order m [35, 36]. These form a 505
form a polynomial sequence of orthogonal polynomials [35]. 506
    For the purpose of this chapter only nonnegative harmonics were used. For each 507
degree Y_{lm} represents the Fourier coefficients capable of reconstructing the spheri- 508
cal harmonic as specified in code written by Moo K. Chung. This code saves the 509
coefficients of the spherical harmonic in a new file for each degree. These can then 510
be reloaded to expedite future calculations [34]. 511
    A final reconstruction is created by iteratively using the desired number of 512
harmonics to reconstruct the original brain in a linear fashion. As each harmonic 513
is loaded into memory, it is multiplied by a factor sigma which is equivalent to the 514
smoothing of the harmonic. A larger sigma value indicates a higher degree of 515
smoothing, while a smaller sigma value preserves more of the data from the current 516
harmonic degree. These values are then linearly added to the previous coordinate 517
value, and the new coordinate is formed. During reconstruction of the original 518
mesh, the surface coordinates can be modeled independently according to the 519
equation: 520

$$v_i(\theta, \varphi) = h_i(\theta, \varphi) + \varepsilon_i(\theta, \varphi), \tag{7.6}$$

where $v_i(\theta, \varphi)$ represents the new coordinate, $h_i(\theta, \varphi)$ represents the original coor- 521
dinate, and $\varepsilon_i(\theta, \varphi)$ is the linear modifier constructed from the combination of the 522
smoothing σ value and the residual Fourier values for the specified coordinate 523
calculated for the current spherical harmonic degree. This procedure is repeated for 524

525 the desired number of harmonics, and a final resulting mesh is produced and
526 returned to the user [37].

527 The error between the reconstructed brain mesh and the original brain mesh is
528 found by calculating the three-dimensional Euclidean distance between
529 corresponding points in the original mesh and the reconstructed mesh. Due to the
530 strict ordering of the data storage in the harmonics, the reconstructed mesh and the
531 original mesh are already registered to one another, and thus do not require
532 additional registration, simplifying the calculations required. Additionally, for
533 visualization purposes, the same connected set of faces is used for both the original
534 and reconstructed mesh [37].

535 All subject data was processed identically, and results were analyzed for σ
536 smoothing values of 0.01, 0.001, 0.0001, and 0.00001. There were 10 subjects in
537 the autistic group and 12 subjects in the non-autistic group. The error for each
538 reconstruction was calculated for every set of harmonics in each of the patients.
539 These errors were then analyzed to find the iteration at which a reconstructed brain
540 demonstrated accuracy below a certain threshold. The thresholds of 11 and 10%
541 were selected for accuracy. Due to the slow convergence of many of the autistic
542 brains, an iteration value of 61 has been used to represent that the brain did not
543 converge below the threshold within the initial 60 iterations used.

544 As the smoothing due to Fourier reconstruction across the mesh is reduced, the
545 amount of data used from each harmonic is increased. The harmonics begin to
546 converge much faster in these reconstructions. The error curves for each data set
547 show the rate of convergence and the maximum convergence visually for a specific
548 brain. The convergence curves at the two extremes for smoothing can be seen in
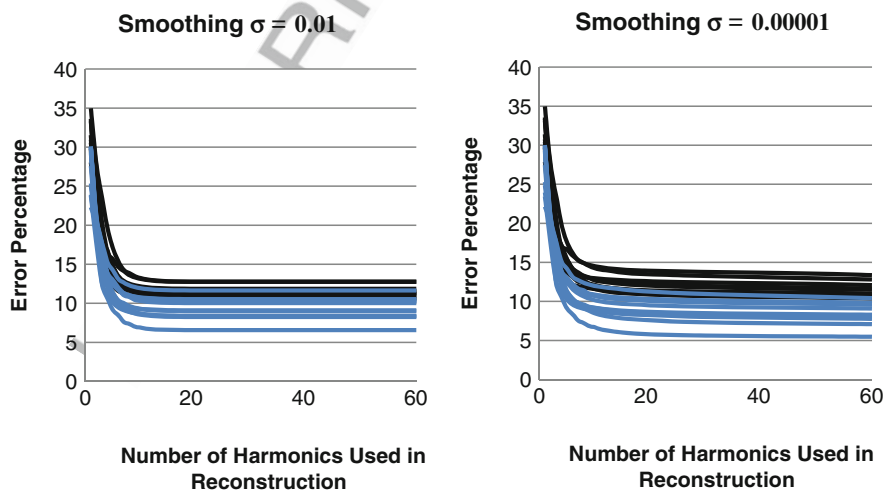549 Fig. 7.12.

Fig. 7.12 Convergence curves for the two extreme values of sigma

7 Shape-Based Detection of Cortex Variability for More Accurate Discrimination

11%Error   10%Error

Analysis using smoothing σ = 0.01

Analysis using smoothing σ = 0.001

Analysis using smoothing σ = 0.0001
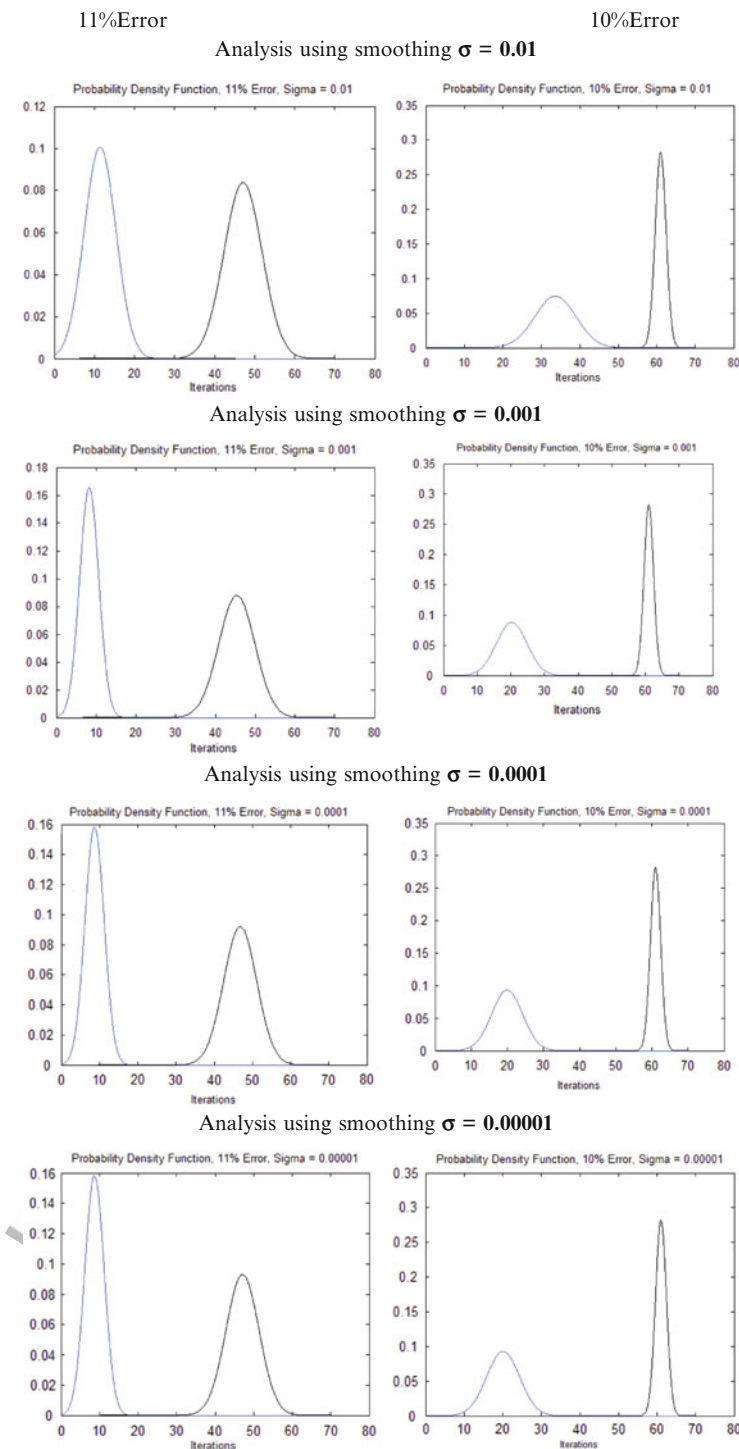

Analysis using smoothing σ = 0.00001

Fig. 7.13 Probability Density Function plots at decreasing levels of σ

It is important to note the overlap between the blue and black lines in the first image in the figure and the sharp distinction between the blue and black lines in the second image. The blue lines represent convergence of subjects not demonstrating autism while the black lines represent subjects who positively demonstrated autistic characteristics.

Probability density functions (pdf) were generated for each error threshold as well using the mean and standard deviation applied to a Gaussian fit pdf. This gives the likelihood of classification for a given number of iterations to convergence. The black lines (right peaks in all images) represent the data for the subjects demonstrating autism while the blue lines (left peaks in all images) represent subjects not demonstrating autism. This shows that the probability of a subject requiring a low number of reconstruction iterations to converge below a given threshold is likely to not be autistic.

7.3 Conclusion and Future Work

Considering the data from previous methods including Modified Checklist for Autism in Toddlers, eye-tracking technologies, and the prevalence of the disorder, it is essential to find alternate and scientific methods that include brain analysis as a diagnostic and evaluative method. The research of doctors at Yale has determined that brain scans can predict the development of autism, leading to early detection and early intervention.

Using this method of analyzing data can demonstrate accurate differences in normal and autistic brains. The research that has been generated in this chapter can clearly demonstrate that the normal brain data converged both faster and with a lower rate of error level than the Autistic brain data. This result proves that the autistic brain is a more complex structure, and would be more difficult to reconstruct using this shape-based detection of cortex variability process.

The flexibility of the created package is of additional importance to the expansion of the project. The algorithms and theories introduced in this chapter can readily be applied to any object freely. The object can be converted from two-dimensional scans into a three-dimensional mesh, deformed and analyzed. This would allow for future analysis of many other organs including cancerous growths and individual components of the brain. Examining the difference between reconstructions can enable change in an object to be tracked over time and compared as well. This would allow for an analysis of the rate of the progression of autism in the individual. This can provide valuable information that can be used to improve treatments by providing physicians with a detailed mathematical representation of the current state of their patient.

It is also plausible to use a technique similar to this one to understand what areas of the brain begin to alter at different times in the subject and to track their impact on the overall autism. Gaining a detailed understanding of the progression of autism in patients can help lead to meaningful solutions for autistic patients.

After numerous attempts to create a package for shape-based detection of cortex 591
variability, the primary difficulties arose in generating an accurate mesh from a 592
variety of data and deforming the mesh into an accurate unit sphere while preserv- 593
ing the integrity and positioning of nodes within the mesh. Through the combina- 594
tion of techniques from a variety of fields including engineering, computer science 595
and graphical art design these challenges were overcome. Using this technique it 596
will be possible to analyze a large variety of MRI scans to compare the complexities 597
of normal and Autistic brains. 598

Future plans are to improve the efficiency of the algorithms to allow accurate 599
deformation and analysis of larger and more detailed mesh structures. Improve- 600
ments in the algorithm will allow for faster and more accurate analysis of the 601
subject. As previously mentioned, it is also planned to make the package more 602
flexible so that it can readily be applied to a variety of structures and used as a 603
meaningful evaluation technique for multiple disorders. 604

References 605

1. Minshew NJ, Payton JB (1988) New perspectives in autism, part I: the clinical spectrum of 606
    autism. Curr Probl Pediatr 18(10):561–610 607
2. Schaefer GB, Mendelsohn NJ (2008) Clinical genetics evaluation in identifying the etiology 608
    of autism spectrum disorders. Genet Med 10(4):301–305 609
3. Losh M, Adolphs R, Poe MD, Couture S, Penn D, Baranek GT, Piven J (2009) Neuropsycho- 610
    logical profile of autism and the broad autism phenotype. Arch Gen Psychiatry 66(5):518–526 611
4. Jacobson JW (2000). Is autism on the rise? Science in Autism, vol 2, no 1 612
5. Rapin I, Tuchman RF (2008) What is new in autism? Curr Opin Neurol 21(2):143–149 613
6. Department of Developmental Services (1999) Changes in the population of persons with 614
    autism and pervasive developmental disorders in California's developmental services system 615
    1987 through 1998. Author, Sacramento, CA 616
7. Department of Education (1999) Digest of education statistics, 1998. Author, Washington, DC 617
    (GPO No. 065-000-01174-3, NCES No. NCES 1999036) 618
8. DiGuiseppi C, Hepburn S, Davis JM, Fidler DJ, Hartway S, Lee NR, Miller L, Ruttenber M, 619
    Robinson C (2010) Screening for autism spectrum disorders in children with Down syndrome: 620
    population prevalence and screening test characteristics. J Dev Behav Pediatr 31(3):181–191 621
9. Stevens M, Fein D, Dunn M, Allen D, Waterhouse LH, Feinstein C, Rapin I (2000) Subgroups 622
    of children with autism by cluster analysis: a longitudinal examination. J Am Acad Child 623
    Adolesc Psychiatry 39:346–352 624
10. Robins DL, Fein D, Barton M, Green J (2001) The modified checklist for autism in toddlers: 625
    an initial study investigating the early detection of autism and pervasive developmental 626
    disorders. J Autism Dev Disord 31(2):131–144 627
11. El-Baz A, Elnakib A, Casanova M, Gimel'farb G, Switala A, Jordan D, Rainey S (2010) 628
    Accurate automated detection of autism related corpus callosum abnormalities. J Med Syst. 629
    doi:10.1007/s10916-010-9510-3 630
12. Abell F, Krams M, Ashburner J, Passingham R, Friston K, Frackowiak R, Happe F, Frith C, 631
    Frith U (1999) The neuro-anatomy of autism: a voxel-based whole brain analysis of structural 632
    scans. Neuroreport 10(8):1647–1651 633
13. Boddaert N, Chabane N, Gervais H, Good CD, Bourgeois M, Plumet MH, Barthelemy C, 634
    Mouren MC, Artiges E, Samson Y, Brunelle F, Frackowiak RSJ, Zilbovicius M (2004) 635

Superior temporal sulcus anatomical abnormalities in childhood autism: a voxel-based morphometry MRI study. Neuroimage 23:364–369

14. Herbert MR, Ziegler DA, Deutsch CK, O'Brien LM, Lange N, Bakardjiev A, Hodgson J, Adrien KT, Steele S, Makris N, Kennedy D, Harris GJ, Caviness VS Jr (2003) Dissociations of cerebral cortex, subcortical and cerebral white matter volumes in autistic boys. Brain 126:1182–1192

15. Egaas B, Courchesne E, Saitoh O (1995) Reduced size of corpus 576 callosum in autism. Arch Neurol 52(8):794–801

16. Schumann CM, Barnes CC, Lord C, Courchesne E (2009) Amygdala enlargement in toddlers with autism related to severity of social and communication impairments. Biol Psychiatry 66(10):942–949

17. Courchesne E, Press GA, Yeung-Courchesne R (1993) Parietal lobe abnormalities detected with MR in patients with infantile autism. AJR Am J Roentgenol 160(2):387–93

18. Schumann CM, Bloss CS, Barnes CC, Wideman GM, Carper RA, Akshoomoff N, Pierce K, Hagler D, Schork N, Lord C, Courchesne E (2010) Longitudinal magnetic resonance imaging study of cortical development through early childhood in autism. J Neurosci 30 (12):4419–4427

19. Kennedy DP, Courchesne E (2008) Functional abnormalities of the default network during self- and other-reflection in autism. Soc Cogn Affect Neurosci 3(2):177–190

20. Hitti M, Chang L (2009) Autism: new clue to earlier detection. WebMD Health News. March 29, 2009

21. Klin A, Lin DJ, Gorrindo P, Ramsay G, Jones W (2009) Two-year-olds with autism orient to non-social contingencies rather than biological motion. Nature 459(7244):257–261

22. Jones W, Klin A (2009) Heterogeneity and homogeneity across the autism spectrum: the role of development. J Am Acad Child Adolesc Psychiatry 48(5):471–473

23. Jones W, Carr K, Klin A (2008) Absence of preferential looking to the eyes of approaching adults predicts level of social disability in 2-year-old toddlers with autism spectrum disorder. Arch Gen Psychiatry 65(8):946–954

24. Gardner A (2010) New hope for early detection of autism. US News: Health Day. May 19, 2010

25. Damasio H, Damasio AR (1989) Lesion analysis in neuropsychology. New York, Oxford

26. Frey R, Woods DL, Knight RT, Scabini D (1987) Defining functional cortical areas with "averaged" CT scans. Soc Neurosci Abstr 13:1266–1267

27. Rorden C, Brett M (2000) Stereotaxic display of brain lesions. Behav Neurol 12(4):191–200

28. Brett M, Leff AP, Rorden C, Ashburner J (2001) Spatial normalization of brain images with focal lesions using cost function masking. Neuroimage 14(2):486–500

29. Fang Q, Boas DA (2009) Tetrahedral mesh generation from volumetric binary and gray-scale images. In: Proceedings of IEEE international symposium on biomedical imaging 2009, pp 1142–1145

30. Fang Q, Carp SA, Selb J, Moore R, Kopans DB, Miller EL, Brooks DH, Boas DA (2008) A multi-modality image reconstruction platform for diffuse optical tomography, Biomedical optics 2008, BIOMED poster session II (BMD), March 2008.

31. Zhang Y, Hamza A (2006) Vertex-based anisotropic smoothing of 3D mesh data, In: IEEE CCECE, pp 202–205

32. Cignoni P, Gobbetti E, Pintus R, Scopigno R (2008) Color enhancement for rapid prototyping. The 9th international symposium on vast international symposium on virtual reality, archaeology and cultural heritage, Eurographics, pp 9–16

33. Pitzalis D, Cignoni P, Menu M, Aitken G (2008) 3D enhanced model from multiple data sources for the analysis of the Cylinder seal of Ibni-Sharrum, The 9th international symposium on VAST international symposium on virtual reality, archaeology and cultural heritage, Eurographics, pp 79–84

34. Fornberg B (1998) A practical guide to pseudospectral methods. Cambridge University Press, Cambridge, UK

35. Chung MK, Shen L, Dalton KM, Evans AC, Davidson RJ (2007) Weighted Fourier represen- 689
    tation and its application to quantifying the amount of gray matter. IEEE Trans Med Imaging 690
    26:566–581   691
36. Courant R, Hilbert D (1953) Methods of mathematical physics, II. Interscience, New York,   692
    English edition   693
37. Chung MK, Dalton KM, Shen LL, Evans AC, Davidson RJ (2007) Weighted Fourier series   694
    representation and its application to quantifying the amount of gray matter. IEEE Trans Med   695
    Imaging 26:566–581   696

Biography

Matthew Nitzken is currently a student of the University of Louisville working on his Ph.D. studies. He holds a B.Eng. and M.Eng. degree in bioengineering from the University of Louisville, Louisville, KY. He has worked on shape analysis and medical imaging studies in his senior and graduate years of the program and plans to pursue this path in his future studies.

Please place Ayman El-Baz's information last in this section.

Ayman El-Baz received the B.Sc. and M.S. degrees in electrical engineering from Mansoura University, Egypt, in 1997 and 2000, respectively and the Ph.D. degree in electrical engineering from University of Louisville, Louisville, KY. He joined the Bioengineering Department, University of Louisville, in August 2006. His current research is focused on developing new computer assisted diagnosis systems for different diseases and brain disorders.

Manuel F. Casanova received his M.D. from the University of Puerto Rico in 1979. He received specialty training in neurology, neuropathology, and psychiatry. In 2003 he came to the University of Louisville where he is the Vice Chair for Research, Department of Psychiatry. His main focus of research is neurodevelopmental conditions, primarily autism.

Fahmi Khalifa received his B.Sc. and M.S. degrees in electrical engineering from Mansoura University, Mansoura, Egypt, in 2003 and 2007, respectively. In May 2009 he joined the BioImaging Laboratory at University of Louisville, Louisville, KY, USA, as a research assistance. His current research is focused on simultaneous image segmentation and registration with main focus on Automatic Diagnosis of Lung Cancer using Contrast Enhancement Computed Tomography Images.

Guela Sokhadze is a Psychology Major, and an undergraduate student of the University of Louisville. As well as working part time at BioImaging Laboratory, he assists at the Cognitive Neuroscience Lab in the Health Sciences Center. He is currently involved in multiple Neuroimaging studies of ADHD and Autism.

Author Queries

Chapter No.: 7

Query Refs.	Details Required	Author's response
AU1	Please check if the name 'Paolo Cignoli' can be replaced with 'Paolo Cignoni' in the sentence 'The mesh was loaded into the freely available software.........'.	Paolo Cignoni is correct. Please replace it.
AU2	The terms 'theta and phi' have been replaced with 'θ and φ' throughout the document. Please check.	These changes are fine.